Indian J. Phys. **77A (2)**, 109–115 (2003)

AN INTERNATIONAL JOURNAL
IJPA

Structure of small and intermediate size silicon clusters

B K Panda
Institute of Physics, Sachivalaya Marg, Bhubaneswar 751 005, Orissa, India
E-mail : bpanda@iopb.res.in

Abstract : Tight-binding molecular dynamics methods are used to optimize geometries of mid-sized silicon clusters up to 23 atoms. The calculated equilibrium structures of the clusters are similar in both orthogonal and nonorthogonal tight-binding simulations. The results obtained in the tight-binding model are compared with those obtained using first principles methods. While in the first principles methods and experiments the structural phase transition is expected to occur at Si_{25} cluster, the tight-binding methods employed in this work predict near-spherical shape for Si_{19}, but prolate structure for Si_{20}. Some properties of these clusters are calculated using tight-binding methods and compared with results obtained from *ab initio* methods.

Keywords : Tight-binding method, molecular dynamics, clusters.

PACS Nos. . 71.15.Fv, 71.15.Pd, 36.40.–c

1. Introduction

Using pulsed laser ablation source the size-selected silicon microstructures were produced and detected by Smalley and coworkers [1] for the first time. Since then several experimental studies such as the Raman scattering [2], infrared spectroscopy [3], photoelectron spectroscopy [4], ion mobility [5], dissociation energy [6] and polarizabilities [7] have been applied recently for understanding the equilibrium structures and properties of these clusters. Unfortunately none of these measurements can directly find the equilibrium geometry of a cluster. Therefore several theoretical methods have been applied to find the geometry of a cluster indirectly from experiments. The theoretical methods include *ab initio* Hartree-Fock methods, density functional methods within the local density approximation (DFT-LDA) and generalized gradient approximation (DFT-GGA) [8]. The tight-binding methods are attractive because of their accuracies and low computational demand [9].

The experiments together with first principles methods [10–14] and tight-binding methods [15–18] have revealed that Si_3, Si_4, Si_5 and Si_7 clusters have isoceles triangle, rhombus, trigonal and pentagonal bipyramids respectively. Although for Si_6 the first principles methods predict two isomers with tetragonal bipyramid and face capped trigonal bipyramid structures, the Raman spectroscopy measurements [2] support tetragonal structure. These compact, multiply coordinated structures are not fragments of the bulk silicon diamond lattice. Their reconstructions are due to the energy gained by tying up the dangling bonds.

The first principles methods [12–14,19] as well as tight-binding methods [15,16,18] without any experimental support have shown that the geometries for clusters with $n = 8$–12 result from the competition between growth patterns based on capping octahedron and trigonal prism isomers of Si_6. The structures for Si_8, Si_9, Si_{10}, Si_{11} and Si_{12} clusters are distorted bicapped octahedron, distorted capped cube, tatracapped trigonal prism, capped trigonal antiprism and hexacapped trigonal prism respectively.

Although several measurements have attempted to understand geometries and properties of these clusters, the most direct information about the structure of these clusters has been obtained by measuring ionic mobilities for their cations [5]. These measurements have revealed that the clusters become prolate between $n = 10$ and $n = 23$, followed

by a structural transition to a more spherical geometry occurring over $n = 24-34$ size range. Since the first principles calculations [5] have shown that the geometries of neutral clusters are the same as their cations, the phase transition from prolate to near-spherical shape for neutral clusters is expected to occur at $n = 25$. The first principles [13,14] and tight-binding calculations [15,16,18] have found that the geometries resulting for $n \leq 18$ are prolate, resembling stacks of nine atom silicon cluster. However, the global minima for $n = 19$ and 20 were very different since the near-spherical geometries are more favoured compared to prolate geometries.

In order to understand this discrepancy Mitas *et al* [21] have performed quantum Monte Carlo calculations and found that the density functional methods based on classical molecular dynamics are not accurate enough for predicting the global minimum. In their calculations the ground state of Si_{20} cluster is found to have prolate structure with Si_9 motif. Rata *et al* [22] have performed global search by the genetic algorithm with the population in each generation having a single parent and suggested some new prolate geometries for $n = 19-23$. Our aim is to verify whether these prolate geometries of silicon clusters for $n = 19-23$ are reproducible in our tight-binding calculations. We have employed our previous orthogonal tight-binding (OTB) [15,16] and nonorthogonal tight-binding (NOTB) [17,18] methods for optimizing geometries of clusters for $n = 19-23$.

In the next section the methods for OTB and NOTB are discussed in brief followed by the results of our calculation and discussion.

2. Tight-binding simulation method

In the tight-binding description of Si bonding, the basis set consists of one s orbital and three p orbitals for each atom. The wave function $Y_k(r)$ for a cluster is expanded as a linear combination of basis functions $F_m(r)$ as [23]

$$\Psi_k(r) = \sum_{\mu i} C^k_{\mu i} \Phi_\mu (r - R_i), \tag{1}$$

where $m = s, p_x, p_y, p_z$ and R_i is the position vector of the i-th atom. The total energy is defined as

$$E = 2\sum E_k + E_{rep} + E_0, \tag{2}$$

where E_k are eigenvalue of the k-th state, E_{rep} is the repulsive energy and E_0 is the adjusted energy shift.

The repulsive energy results from the repulsion due to ions as wel as the correction for double counting of the exchange-correlation energy. The repulsive energy is expressed in terms of pair repulsive potential f as

$$E_{rep} = \sum_i \sum_{j>i} \phi(R_{ij}), \tag{3}$$

where $R_{ij} = R_i - R_j$. Both eigenvalues (E_k) and wave function coefficients (C^k) are obtained by solving the Schrödinger equation. The characteristic equation in the matrix form becomes

$$\sum_{\mu,\nu} \left[H_{\mu,\nu}(R_{ij}) - E_k S_{\mu,\nu}(R_{ij}) \right] C^k_{\nu j} = 0. \tag{4}$$

The hopping integrals are described as

$$H_{\mu,\nu}(R_{ij}) = \int \Phi^*_\mu (r - R_i) H \Phi_\nu (r - R_j) d^3 r. \tag{5}$$

The overlap matrix elements are given as

$$S_{\mu,\nu}(R_{ij}) = \int \Phi^*_\mu (r - R_i) \Phi_\nu (r - R_j) d^3 r. \tag{6}$$

The evaluation of H and S matrices needs atomic wave functions F_m which are usually calculated in the tight-binding density functional method [20]. For molecular dynamics simulations such a method in quite involved. We have therefore followed empirical methods where the matrix elements of H and S are expressed in the functional form of the interparticle separation by a set of four Slater-Koster parameters [23] usually obtained from a first principles method. In the (s,p) representations the elements of the Hamiltonian $H_{m,\nu}$ are described by two-center Slater-Koster parameters V_{sss}, V_{sps}, V_{pps} and V_{ppp} with the direction cosines of the vectors joining atoms. Similarly the elements of the overlap matrix are described by Slater-Koster parameters S_{sss}, S_{sps}, S_{pps} and S_{ppp}. The on-site energies for s and p states are represented by $\hat{I}_s$ and $\hat{I}_p$ respectively.

In the following we describe both orthogonal and nonorthogonal methods employed in this work.

2.1. *Semi-empirical orthogonal tight-binding method*.

The parameters in the semi-empirical OTB method have been derived taking several results from both the DFT-GGA calculations and experiments [24]. In the OTB method, the overlap integral is taken a unit matrix $S = I$ so that

$$\left[H_{\mu,\nu}(R_{ij}) - \delta_{\mu,\nu}\delta_{i,j} E_k \right] C^k_{\nu,j} = 0. \tag{7}$$

In this method, the transferable Slater-Koster parameters V_{lm1} and pair repulsive potential $f(r)$ are represented by the cubic-splines. The on-site energies $\hat{I}_s$ and $\hat{I}_p$ are made equal and opposite in order to get rid of the adjustable parameter E_0.

2.2. *Empirical non-orthogonal tight-binding method* :

The nonorthogonal tight-binding potentials and overlap matrix elements are taken from the work of Menon-Subbaswamy [17] which is based on the Hückel method [25,26]. The matrix elements of the Hamiltonian in the non-orthogonal scheme H_{mn} are constructed from the Slater-Koster parameters V_{mn1} in the same way as in the OTB

scheme according to the prescription given by Schilfgaarde and Harrison [26],

$$H_{\mu,\nu}(R_{ij}) = V_{\mu\nu\lambda}(R_{ij})\left[1+\frac{1}{K(R_{ij})}-S_2^2(R_{ij})\right], \quad (8)$$

where S_2 is the non-orthogonality between the sp^3 hybrids,

$$S_2 = \frac{\left(S_{ss\sigma}-2\sqrt{3}S_{sp\sigma}-3S_{pp\sigma}\right)}{4} \quad (9)$$

The parameter $K(r)$ used for transferability is defined as

$$K(r) = K_0 e^{\sigma(r-d_0)}. \quad (10)$$

The Slater-Koster two-center integrals $V_{lm\mu}$ are taken to decrease exponentially with r,

$$V_{lm\lambda}(r) = V_{lm\lambda}(d_0)e^{-\alpha(r-d_0)}. \quad (11)$$

The quantities $S_{lm\mu}$ are determined from $V_{lm\lambda}$ in the Hückel method as,

$$S_{lm\lambda}(r) = \frac{2V_{lm\lambda}(r)}{K(r)(\epsilon_l+\epsilon_m)}. \quad (12)$$

As in eq. (11), the scaling laws of the repulsive potential are taken to be exponential in nature :

$$\phi(r) = \phi(d_0)e^{-\beta(r-d_0)}. \quad (13)$$

The input parameters are taken from the work on Menon-Subbaswamy [17].

2.3 *Molecular dynamics simulations :*

In order to optimize cluster geometries, the atomic positions in the classical molecular dynamics scheme are updated as

$$R_n(t+\delta t) = R_n(t)+v_n(t)\delta t+\frac{1}{2}a_n(t)(\delta t)^2, \quad (14)$$

where $a_n = F_n/m$ with m being the mass of Si atom. The force on n-th atom is calculated as

$$F_n = -2\sum_k\sum_{\mu i}\sum_{\nu j}\left\{C^{*k}_{\mu i}\frac{\partial H}{\partial R_n}-E_k\frac{\partial S}{\partial R_n}C^k_{\nu j}\right\} - \frac{E_{rep}}{\partial R_n}. \quad (15)$$

For the OTB method the derivative involving S vanishes. The first and second terms correspond to forces due to attractive electronic and repulsive terms respectively. The electronic forces are calculated taking the Hellman-Feynman theorem. The velocity of the n-th atom at time t is calculated using the velocity-verlet scheme [9]

$$v_n(t) = \frac{1}{2}[a_n(t)+a_n(t-\delta t)]\delta t. \quad (16)$$

For simulated annealing we have used the quenching methods which optimizes clusters with symmetry constraints [15].

3. Results and discussion

The total energy of a cluster containing a given number of silicon atoms has been calculated using the method described above. The forces on each atom are calculated allowing the atoms to move in the molecular dynamics algorithm until the forces become negligibly small. For larger clusters we have started from many different initial geometries and arrived in this way to the minimum energy configuration. The details for the cluster geometries and their properties up to n = 18 have been reported in our previous works using OTB and NOTB methods [15,16,18]. Both OTB and NOTB methods yield similar low lying structures for all cluster geometries studied here. The cluster geometries for n = 19–23 are shown in Figure 1. Three different isomers

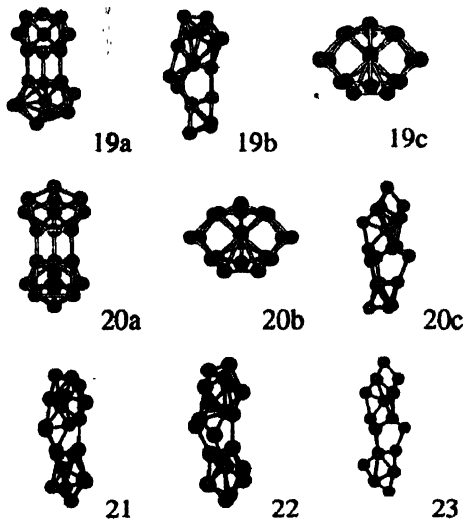

Figure 1. Silicon clusters for sizes n = 19–23 obtained using tight-binding molecular dynamics methods. Three isomers are shown for Si_{19} and Si_{20} clusters.

have been presented for Si_{19} and Si_{20} clusters. The structures 19a and 20a which resemble the prolate structures for n = 14–18 with Si_9 motif are taken from the work of Ho *et al* [5]. The compact cage-like structures 19c and 20b which are found as the low lying structures in the DFT-LDA schemes are taken from the work of *Ho et al* [5]. The prolate structures 19b and 20c are taken from the genetic algorithm search of Rata *et al* [22]. These structures do not have Si_9 motif as in 19a and 20a. From Figure 1 it is found that Si_{19b}, Si_{20c}, Si_{21}, Si_{22} and Si_{23} clusters take similar prolate structures.

In order to find the best structure for Si_{19} and Si_{20} clusters, their cohesive energies are reported in Table 1.

In Table 1, the geometry of Si_{19} cluster in both OTB and NOTB methods is found to take cage-like structure. On the other hand, the geometry of the Si_{20} cluster takes prolate structure. Although the low lying geometry for Si_{19} in our

Table 1. Cohesive energies for silicon clusters with 19 and 20 atoms for different isomers shown in Figure 1.

Size	OTB (eV)	NOTB (eV)
19a	3.738	4.122
19b	3.741	4.121
19c	3.762	4.163
20a	3.731	4.097
20b	3.739	4.128
20c	3.749	7.137

case does not agree with that obtained by Rata *et al* [22], it is surprising that Si_{19} cluster shows cage-like shape ahead of Si_{20}. It is quite natural that Si_{19} should take prolate structure. The ion mobility measurements [5] suggest that the phase transition from prolate to cage-like structures occurs at $n = 25$. The quantum Monte Carlo method suggests that the formation probability for a cage-like structure is quite formidable as it requires many subunits of small clusters. We therefore assume that the geometry of Si_{19} cluster neither takes the structure 19a with Si_9 motif nor the structure 19b which resembles the shape of higher clusters. At this size the cluster geometry takes a shape transition which needs further optimizations.

The calculated cohesive energies using OTB and NOTB methods together with those obtained in the DFT-LDA [14] and DFT-GGA methods [14,22] are shown in Figure 2.

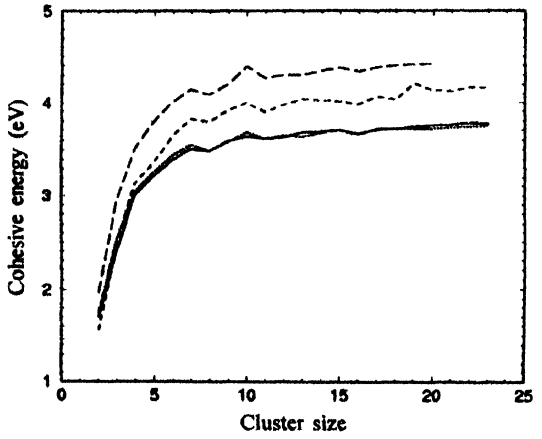

Figure 2. Cohesive energy as a function of cluster size. Notations for different methods, solid line (CP-GGA), long-dashed line (CP-LDA), dashed line (OTB) and dotted line (NOTB). For Si_{19} and Si_{20} clusters 19c and 20c geometries shown in Figure 1 are taken here.

As shown in Figure 2, the cohesive energies increase with cluster size rapidly up to $n \leq 10$ and then the size dependence becomes smooth at $n = 9-11$. Such behaviour can be related to the transition of the equilibrium geometries from capped structures to prolate structures. The cohesive energies evaluated in the OTB method are close to those of DFT-GGA method since the parameters in the OTB method are carefully derived from the DFT-GGA scheme. The empirical NOTB method finds cohesive energies lying between DFT-LDA and DFT-GGA values. The cohesive energy of the bulk silicon is 4.48 eV. The cohesive energies obtained in the DFT-LDA method are higher than bulk limit which clearly shows that LDA overbinds the atoms in a cluster and the gradient corrections are quite essential for calculating their correct values.

The magic clusters are the most stable structures with higher cohesive energies than their neighbours. The occurrence of kinks for cluster sizes 4, 7 and 10 atoms clearly indicates that these are magic clusters which also agree with measurements [27]. In order to find other magic clusters, the fragmentation spectra are calculated taking the second difference of cluster energies as

$$\Delta_2 E_n = E(n+1) + E(n-1) - 2E(n). \tag{17}$$

In Figure 3, the calculated fragmentation spectra obtained in the OTB and NOTB methods are compared with those obtained in the DFT-LDA and DFT-GGA schemes.

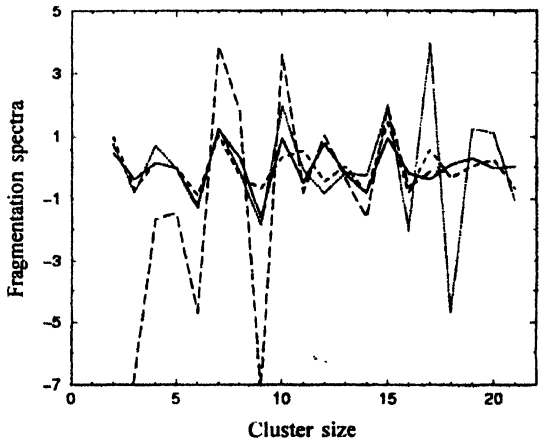

Figure 3. Fragmentation spectra as a function of cluster size. Notations for different methods are same as in Figure 2.

Maxima are found at $n = 4, 7, 10, 15, 17, 20$, implying that these are magic clusters since these are more stable than their neighbouring clusters. The magic clusters at 4, 7 and 10 resemble those found for Ge clusters. The relative stability of these clusters can be explained in light of the details of their equilibrium structures. Since Si_7 and Si_{10} are magic clusters, it is easy to understand that Si_{17} cluster constructed by these clusters is also a magic cluster. The important properties of these magic clusters are that there are not only several isomers for magic clusters, but also the bond lengths for these clusters are long [28]. Several isoenergetic isomers result for magic clusters due to the flatness of energy hypersurface at the minimum. Since the cohesive energy is high when the bond lengths are short, the long bond lengths for these clusters are not intiutively understood.

The closed-shell and open-shell patterns of the electronic configuration are generally identified with large and small energy gaps respectively which is defined as the energy difference between highest occupied molecular orbital (HOMO) and lowest unoccupied molecular orbital (LUMO). In Figure 4 we have compared energy gaps of Si clusters obtained using tight-binding methods with DFT methods.

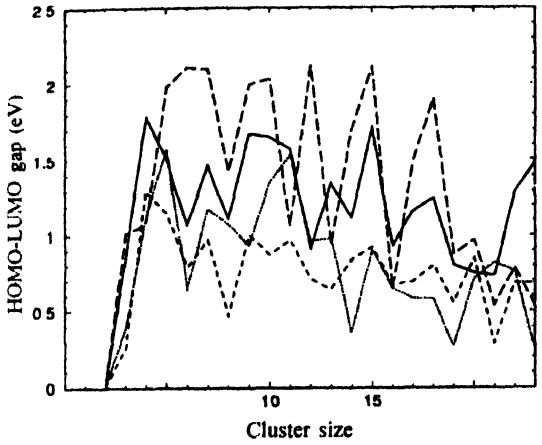

Figure 4. HOMO-LUMO gap (eV) of silicon clusters. Notations for different methods are same as in Figure 2.

As shown in Figure 4, the energy gaps are largest in the DFT-LDA method while they are very small in the OTB method. However, with exception to the NOTB method the size dependent trend in the DFT-LDA, DFT-GGA and OTB methods are quite similar. Recently, Müller *et al* [29] have estimated the HOMO-LUMO gaps of silicon clusters from measured photoelectron spectra. Unfortunately none of these methods correctly predict the magnitudes and size dependent trend found in measurements [29]. In metallic clusters the energy gap normally decreases with increasing size as a consequence of electronic level quantization in a cavity. In Si clusters the general trend in all theoretical methods predict that the energy gaps decreasing with increasing cluster size as a result of highly coordinated bonding. Unfortunately the energy gaps estimated from measurements do not agree with the theoretical predictions as these increase with increasing n. However it has been experimentally and theoretically observed in Ge clusters that the gaps decrease with increasing n similar to our theoretical predictions [30]. The measurements predict that clusters with 7, 9, 15, 18 atoms are closed shell species while 6, 8, 13 and 16 atoms are open-shell species in agreement with our calculations.

The polarizability is useful for a cluster as it is a basic property of the electronic systems. It has been measured for small Si_n (n = 4–120) by Schäfer and co-workers. Before calculating the polarizabilities of clusters it is worth finding the bulk limit of it using the Claussius-Mossotti relations,

$$\bar{\alpha} = \frac{3}{4\pi}\left(\frac{\epsilon-1}{\epsilon+1}\right)\upsilon_{at}, \tag{18}$$

where υ_{at} is the volume per Si atom in the Si unit cell and ϵ is the static dielectric constant of the bulk. The bulk atomic polarizability is estimated from this expression as 3.71 Å^3/atom. The measured polarizabilities per atom are systematically lower than the bulk limit.

The definition of the polarizability per atom in the one-electron perturbation theory yields,

$$\alpha_x = 2e^2 \sum_{k,l} \frac{|D_{kl}^x|}{E_l - E_k} \tag{19}$$

where E_k and E_l are the single particle energies in the occupied and unoccupied levels respectively. The dipole matrix elements D_{kl}^x along x-direction are defined as,

$$D_{kl}^x = \int \Psi_k^*(r) R_n^x \Psi_l(r) d^3 \tag{20}$$

where $\Psi_k(r)$ and $\Psi_l(r)$ are occupied and unoccupied orbitals respectively. In the diagonal ansatz D_{kl}^x is derived by substituting eq. (1) in eq. (20) as, substituting eq. (1) in eq. (2), D_{kl}^x is derived as [31]

$$D_{kl}^x = \sum_{\mu,l} C_{\mu l}^{k*} C_{\mu l}^l R_n^x + \sum_{\mu,l}\sum_{\nu,l} C_{\mu l}^{k*} C_{\nu l}^l d_{\mu\nu}^x . \tag{21}$$

The first term is calculated in the diagonal ansatz and the second term includes off-diagonal terms with the intra-atomic dipole matrix,

$$d_{\mu\nu}^x = \int \phi_\mu(r) x \phi_\nu(r) d^3 r . \tag{22}$$

The off-diagonal term is neglected in our work. The average polarizability per atom is then given by the invariant trace $<\alpha> = \frac{1}{3}(\alpha_{xx} + \alpha_{yy} + \alpha_{zz})$.

Focusing on the energy denominator in eq. (19), this expression suggests that $<\alpha>$ should be inversely proportional to HOMO-LUMO energy gap. However, Vasiliev *et al* [12] have pointed out that contributions from transition above the energy gap can dominate this expression and the relationship between $<\alpha>$ and energy gap does not hold in general. In Figure 5, the calculated polarizabilities for Si_n clusters (n = 2–23) are compared with those obtained using the DFT-LDA schemes [32,33].

Unfortunately the polarizabilities for the DFT-GGA scheme are not available for comparison. However, the magnitudes of polarizabilities are expected to decrease since the transition energy spacings are generally increased by

this correction. As shown in Figure 5, the DFT-LDA and NOTB methods yield similar $<\alpha>$ which lie above the bulk limit. On the other hand, the $<\alpha>$ found in the OTB method

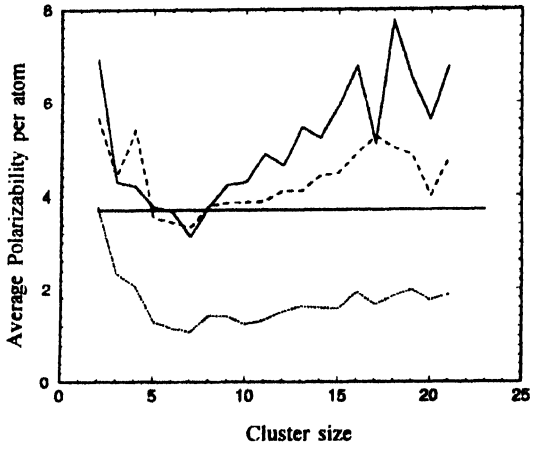

Figure 5. Polarizabilities per atom of silicon clusters. Notations for different methods are same as in Figure 2. The bulk limit is shown by a solid line.

are lower than the bulk limit which suggests that the NOTB method is more appropriate for $<\alpha>$ calculation since the overlap matrices are included in this formalism. The only way to improve the magnitudes of polarizabilities is to include intra-atomic dipole matrix elements [31]. Nevertheless, the measured polarizabilities lie below the bulk limit which cannot be explained by any theory applied so far.

4. Conclusions

We have simulated geometries of neutral clusters up to $n = 23$ using both OTB and NOTB methods. Although cohesive energies in the OTB method are very close to those obtained using the DFT-GGA method, the hopping integrals are found to be unphysical since they do not preserve signs with increase in the interparticle separation. One possible reason for this is that all OTB methods require environmental corrections [16,34] when they are calculated from the NOTB methods which is not taken here. On the other hand, the NOTB method does not require this correction. The magic clusters require further analysis for understanding their abnormal behaviour. The fragmentation spectra and energy gaps calculated in the OTB method agree qualitatively with those found in DFT. However, the polarizabilities found in the NOTB method agree with DFT-LDA methods.

Acknowledgment

The author would like to thank Professor S N Behera for valuable discussions.

References

[1] J B Hopkins, P R R Landridge-Smith, M D Morse an R E Smalley *J. Chem. Phys.* **78** 1627 (1983)

[2] E C Honea, A Ogura, C A Murray, K Raghavachar W O Sprenger, M F Jarrold and W L Brown *Nature* (Londo 366 42 (1993); Honea *et al, J. Chem. Phys.* **110** 12161 (199

[3] S Li, R J Van Zee, W Weltner (Jr.) and K Raghavachari *Che Phys. Lett.* **243** 275 (1995)

[4] C Xu, T R Taylor, G R Burton and D M Neumark *J Che Phys.* **108** 1395 (1998)

[5] K M Ho, A A Shvartsburg, B Pan, Z Y Lu, C Z Wan G W Wacker, J L Fye and M F Jarrold *Nature* (London) 39 582 (1998)

[6] A A Shvartsburg, M F Jarrold, B Liu, Z-Y Lu, C Z Wan and K M Ho *Phys. Rev. Lett.* **81** 4616 (1998)

[7] R Schaäfer, S Schlecht, J Woenckhaus and J A Becker *Phy Rev. Lett.* **76** 471 (1996)

[8] *Microclusters* (ed.) S Sugano, Y Nishina and S Ohnishi (Springe Berlin) (1987)

[9] L Colombo *Annual Reviews of Computational Physics* Vol. I (ed.) D Stauffer (World Scientific, Singapore) (1996 K Raghavachari and C M Rohlfing *J. Chem. Phys.* **89** 221 (1988)

[10] K Raghavachari and C M Rohlfing *J. Chem. Phys.* **89** 221 (1988)

[11] R Fournier, S B Sinnot and A E DePristo *J Chem. Phys* 9 4149 (1992)

[12] I Vasiliv, S Ögüt and J R Chelikowsky *Phys. Rev. Lett.* **78** 480 (1997)

[13] B Liu, Z Y Lu, B Pan, C Z Wang, K M Ho, A A Shvartsbur and M F Jarrold *J. Chem. Phys.* **109** 9401 (1998)

[14] A A Shvartsburg, B Liu, M F Jarrold and K M Ho *J. Chem Phys.* **112** 4517 (2000)

[15] B K Panda, S Mukherjee and S N Behera *Phys. Rev.* **B63** 4540 (2001)

[16] S N Behera, B K Panda, S Mukherjee and P Entel *Phase Tran* **75** 41 (2001)

[17] M Menon and K Subbaswamy *Phys. Rev.* **B55** 9231 (1997)

[18] S N Behera, B K Panda, S Mukherjee and P Entel (unpublished

[19] C M Rohlfing and K Raghavachari *Chem. Phy. Lett.* **167** 55 (1990)

[20] Th Frauenheim, F Weich, Th Köhler, S Uhlmann, D Porezag an G Seifert *Phys. Rev.* **B52** 11492 (1995)

[21] L Mitas, J C Grossmas, I Stich and J Tobik *Phys. Rev. Lett.* **8** 1479 (2000)

[22] I Rata, A A Alexandre, A Shvartsburg, M Horoi, T Frauenheim K W M Siu and K A Jackson *Phys. Rev. Lett.* **85** 546 (2000)

[23] J C Slater and G F Koster *Phys. Rev.* **94** 1498 (1954)

[24] T J Lenosky, J D Kress, I Kwon, A F Voter, B Edward D F Richards, S Yang and J B Adams *Phys. Rev.* **B55** 152 (1997)

[25] R Hoffmann *J. Chem. Phys.* **39** 1397 (1963)

[26] M van Schilfgaarde and W A Harrison *J. Phys. Chem. Solids* 4 1093 (1985)

[27] L A Bloomfield, R R Freeman and W L Brown *Phys. Rev. Lett* **54** 2246 (1985)

[28] A D Zdetsis *Phys. Rev.* **A64** 023202 (2001)

[29] J Müller, B Liu, A A Shvartsburg, S Ogut, J R Chelikowsky, K W M Siu, K M Ho and G Gantefor *Phys. Rev. Lett* **85** 1666 (2000)

[30] J Wang, G Wang and J Zhao *Phys. Rev* **B64** 205411 (2001)

[31] Th G Pedersen, K Pedersen and Th B Kriestensen *Phys. Rev.* **B63** 201101 (2001)

[32] K Jackson, M Pederson, C-Z Wang and K-M Ho *Phys. Rev* **A59** 3685 (1999)

[33] K Deng, J Wang and C T Chan *Phys Rev* **A61** 025201 (2000)

[34] D Nguyen-Manh, D G Pettifor and V Vitak *Phys Rev Lett* **85** 4136 (2000)